Raman imaging through multimode sapphire fiber

SUNAN DENG,[1,2] DAMIEN LOTERIE,[1] GEORGIA KONSTANTINOU,[1] DEMETRI PSALTIS,[3] AND CHRISTOPHE MOSER[1,*]

[1]*Ecole Polytechnique Fédérale de Lausanne, Laboratory of Applied Photonics Devices, CH-1015 Lausanne, Switzerland*
[2]*Baidu Shenzhen R&D Center, Baidu International Building, Xuefu Road East, Nanshan District, ShenZhen,518000, China*
[3]*Ecole Polytechnique Fédérale de Lausanne, Laboratory of Optics, CH-1015 Lausanne, Switzerland*
[*]*christophe.moser@epfl.ch*

Abstract: We report on a sapphire fiber Raman imaging probe's use for challenging applications where access is severely restricted. Small-dimension Raman probes have been developed previously for various clinical applications because they show great capability for diagnosing disease states in bodily fluids, cells, and tissues. However, applications of these sub-millimeter diameter Raman probes were constrained by two factors: first, it is difficult to incorporate filters and focusing optics at such small scale; second, the weak Raman signal is often obscured by strong background noise from the fiber probe material, especially the most commonly used silica, which has a strong broad background noise in low wavenumbers (<500-1700 cm^{-1}). Here, we demonstrate the thinnest-known imaging Raman probe with a 60 µm diameter Sapphire multimode fiber in which both excitation and signal collection pass through. This probe takes advantage of the low fluorescence and narrow Raman peaks of Sapphire, its inherent high temperature and corrosion resistance, and large numerical aperture (NA). Raman images of Polystyrene beads, carbon nanotubes, and $CaSO_4$ agglomerations are obtained with a spatial resolution of 1 µm and a field of view of 30 µm. Our imaging results show that single polystyrene bead (~15 µm diameter) can be differentiated from a mixture with $CaSO_4$ agglomerations, which has a close Raman shift.

1. Introduction

Raman spectroscopy is a powerful analytical tool to detect the frequency shift in the inelastic light scattering due to the molecular vibrational modes in a sample [1,2]. Raman detection is a label-free method [3], thus greatly simplifying the sample preparation and minimally disturbing the sample during detection [4]. It has found a myriad of applications ranging from detection of biohazard contaminants [5], monitoring biological processes [6], disease diagnosis [7], to regenerative medicine [8].

Fiber Raman probes are a crucial device for challenging applications where access is severely restricted [9], for example, detection of hidden illegal drugs, toxic material analysis, and high temperature sensing [10]. Small dimension Raman probes have been developed for various clinical applications as they show great potential for diagnosing disease states in bodily fluids, cells, and tissues [11]. Raman probes have been developed with probe diameters, ranging from the centimeter [12] scale, millimeter scale and sub-millimeter [13,14] scale. Although small scale probes enable new applications, either adapting to endoscopy [15] or working as needle probe [16], their optical design are constrained by the difficulty of incorporating filters and lenses at this scale.

Another challenge in the development of small Raman probes is the weak signal from the sample that is often obscured by fluorescence and Raman background from the probe material [17]. Thus, despite that Raman imaging with single silica probe as small as 125 µm has been

realized in a multimode fiber with a transmission matrix correction [18], strong background from the silica fiber itself at lower wavenumbers (<500-1700 cm^{-1}) confines the detection to the higher wavelength number regime (>2500 cm^{-1}). However, in clinical applications, most prominent Raman shifts are assigned to the aromatic amino acid phenylalanine (1,004 cm^{-1}), unsaturated fatty acids (1,267 and 1,661 cm^{-1}), CH_2 and CH_3 deformation vibrations (1,301 and 1,445 cm^{-1}), and the amide bands of protein backbones (1,267 and 1,661 cm^{-1}), all of them occurring in the low wavenumber range [19]. In addition, most compounds resulting from corrosion such as for example, Wustite, Hematite, and Magnetite have Raman wavenumber smaller than 1700 cm^{-1} [20].

A sapphire optical fiber, with its inherent low background noise due to its crystalline nature allows detection and imaging in a broad frequency range (>800 cm^{-1}). It has proven to have a clear advantage over silica for Raman spectroscopy [9]. Furthermore, the sapphire fiber can also be used for high temperature sensing due to its high melting point(~2053°C) and corrosion resistance [10]. However, to the best of our knowledge, no sapphire fiber Raman imaging has been demonstrated.

Here we propose and demonstrate a very thin Raman imaging probe based on a 60 μm diameter multimode sapphire optical fiber (air cladding) for both the excitation and collection of Raman signal, without any additional focusing optics. The wave front control was performed by digital phase conjugation method [21–23], which has potentially shorter response time than the transmission matrix method [24,25] since no measurement of the matrix elements [26] is needed. The sapphire air-clad fiber with a theoretical numerical aperture (NA) of 1 is expected to have a high collection efficiency.

We demonstrate the capability of our approach for a Raman imaging probe by imaging and detecting polystyrene beads, carbon nanotube (CNT) paper, and $CaSO_4$ agglomerations. Our results show that single polystyrene bead (~15 µm diameter) can be differentiated from a mixture with $CaSO_4$ agglomerations, which has a close Raman shift.

2. Materials and methods

2.1 Experimental setup

The experimental setup is illustrated in Fig. 1. The output beam of a 532 nm wavelength laser (Verdi-10V, Coherent, Santa Clara, CA) was expanded using a telescope (lens L1 with f = 30mm, L2 with f = 150mm) and projected onto a polarized beam splitter PBS1, which divides the light into two arms, one to be delivered to the fiber (object beam) and the other to be used as the reference beam for the holographic recording. The ratio of the two beams can be adjusted by a half-waveplate. The object beam contains the sapphire fiber (MicroMaterials, Inc., 5 cm long with 60 μm core).

In the object beam, light is focused through a 60X microscope objective (NA = 0.85, OBJ2) onto the sapphire fiber facet. The generated focus is then coupled into the propagation modes of the fiber and generates a random speckle pattern at the output facet. The speckle pattern is imaged on camera 1 (Photonfocus MV1-D1312 (IE)-G2, CMOS camera) through a 60X objective (NA = 0.85, OBJ1) and a lens L3 (f = 300mm). The reference beam is directed towards the imaging plane through reflection by the beam splitter BS1(R50:T50) thus generating an off-axis hologram. The recorded hologram is then processed numerically and the phase of the optical field on the output facet of the fiber is retrieved.

The recording of the hologram is the calibration procedure. After this, the object beam is blocked to carry on the reconstruction process. The recorded hologram is digitized and the phase of the incident wave front is calculated by computer (Fourier Transform) before being sent to a phase-only spatial light modulator (Pluto-NIR II, Holoeye). Then, the incident light (reference beam) is modulated and reflected through beam splitter BS1 and projected onto the fiber facet through L3 and OBJ1 to generate a digital phase conjugated focal spot on the other end of the fiber. The process is also called off-axis hologram reconstruction [27].

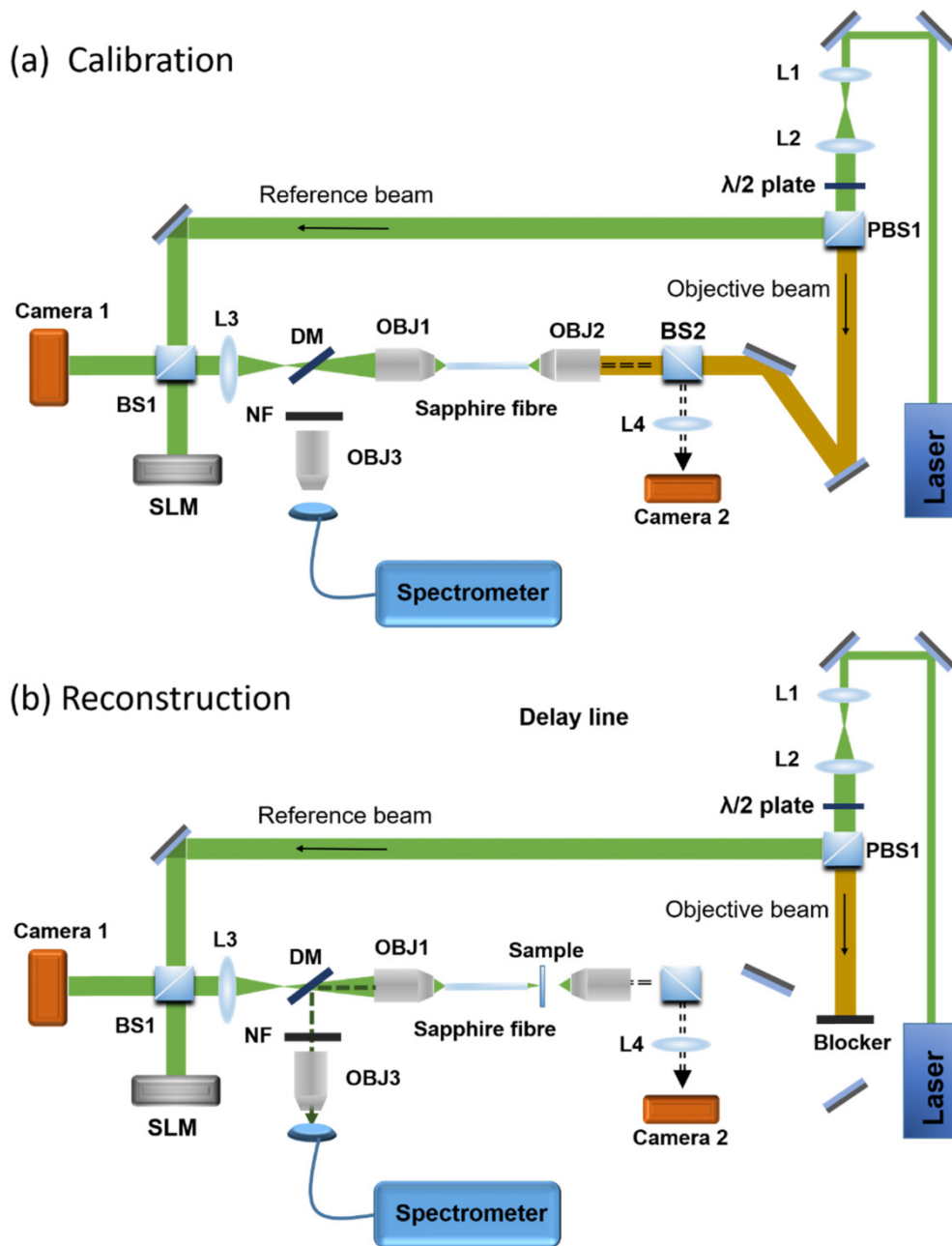## (a) Calibration

(b) Reconstruction

Fig. 1. Experimental Setup. The beam is expanded by the telescope formed by lenses L1-L2 and is split in two arms with the polarizing beam splitter PBS1. The other beam is focused on the sapphire fiber facet with the objective OBJ2. The output of the fiber is imaged on the CMOS sensor through the 4f imaging system (OBJ1 and L3). The reference beam is combined with the image by reflecting on the non-polarizing beam splitter BS1 to generate a hologram. The phase conjugation beam is generated by the reference beam reading out the computed phase pattern loaded onto the SLM. The phase pattern was obtained by Fourier transform. The phase conjugation beam is redirected towards the fiber by reflecting again on BS1. The quality of the generated focus is examined by the imaging system composed by OBJ2, BS2 and L4 on camera 2 in reflection.

The alignment process is very critical on the final efficiency of the digital phase conjugation (DPC) system. The sensor and the SLM need to be aligned pixel by pixel to form the correct phase conjugate beam. The DPC spot can be viewed through the imaging system composed by objective OBJ2 and lens L4 on camera 2 (Baumer TXF-14 CCD camera).
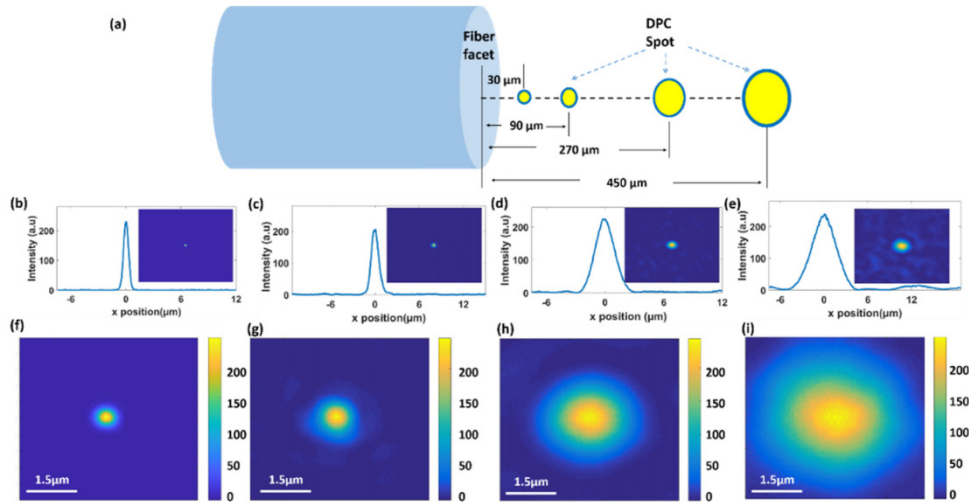

Fig. 2. (a) Schematic of DPC spots with difference distances from the sapphire fiber face. (b-e) DPC spot beam shape on the fiber axis at 30 μm, 90 μm, 270 μm, and 450 μm away from the facet, respectively. (f-i) enlarged images of corresponding spots at 30 μm, 90 μm, 270 μm, and 450 μm from the fiberwith spot sizes 0.63 μm, 1.01 μm, 2.03 μm, and 3.33 μm. The sizes was calculated by the full width at half maximum of curves in (b)-(e).

As is expected, the DPC spots enhancement decreases with increasing distance from the fiber facet, as shown in Fig. 2(a). The enhancement is calculated by the ratio of the peak intensity and the average background. When the DPC spot is 90 μm, 270 μm, and 450 μm away from the fiber facet, the enhancement is 1184,208,94 respectively. Meanwhile, when the enhancement decreases, the size of the DPC spots becomes larger, shown as the intensity curves cross the middle of the spots in Fig. 2(c)- 2(e), as well as the enlarged spots images in Fig. 2(g) -2(i).

In this work, the DPC spot was set 30 μm away from the fiber facet. The spot, shown in Fig. 2(b) and 2(f) has an enhancement of 2106, spot size 0.63 μm.

2.2 Sample preparation and detection

Polystyrene beads: A suspension of polystyrene beads (Thermo Scientific 7510A, 11 μm mean diameter, ≤ 18% coefficient of variation) was placed on a standard glass coverslip (Sigma, 24 mm × 60 mm) and dried to form agglomerations.

Calcium sulfate agglomerations: 5 mg calcium sulfate power (Sigma 7778-18-9, $CaSO_4$, ≥99.99%) was dispersed in 30 μl water. Then the solution was placed on a standard glass coverslip (Sigma, 24 mm × 60 mm) and dried to form agglomerations.

Carbon nanotube paper: CNT paper [28], with a thickness of 70 μm, was fabricated by multiple steps of SWCNT dispersion and suspension filtration. Our dispersion method consisted of two steps: (1) 1 g SWCNT mixed with 5 g Triton X-100 was dispersed by a three-roller shear disperser (DS50, EXAKT) for 20 min; (2) The mixture in step (1) was dissolved in 5 L deionized water and dispersed by dynamic sonication using a high-power ultrasonic processor (Vibra-CellTM, Sonics) circulated twice. Then the homogeneous solution from the dispersion process was vacuum filtered onto a membrane with a pore size of 1 μm to form a SWCNT film. Finally, the as prepared film was heated at 90 °C for 5 h and peeled from the filter membrane [28].

3. Experiments

Contrary to a silica fiber, which gives a strong broad spectral background, a sapphire fiber has only several sharp Raman peaks, with low background, as demonstrated in Fig. 3. Sapphire crystal belongs to space group D_{3d}^6 and has irreducible representation for the optical modes of $\Gamma = 2A_{1g} + 2A_{1u} + 3A_{2g} + 2A_{2u} + 5E_g + 4E_u$ [10]. However, the Raman active transitions are the two A_{1g} and five E_g modes, corresponding to Raman shifts 379, 418, 431, 450, 578, 645, and 750 cm^{-1}. When no sample is added at the tip of the fiber, the spectrum of the sapphire fiber was detected in reflection and shown in Fig. 3.

   Based on this measurement, the sapphire fiber could detect materials having Raman shifts in the very low range, such as 0-300 cm^{-1}, as well in between 500 and 700 cm^{-1}. In this work, we focused on materials with Raman shift in the range of 900-1600 cm^{-1}, a range in which a silica multimode fiber could not be used due to the strong background noise.
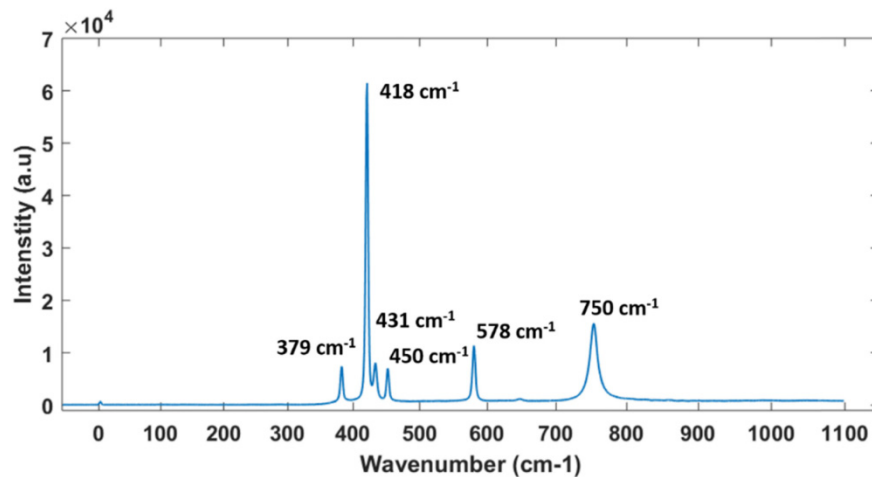

Fig. 3. Raman signal from sapphire fiber. The spectrum was taken when the DPC spot is on the fiber facet, with the object beam blocked. The illumination light is 532 nm wavelength laser (Verdi-10V, Coherent, Santa Clara, CA), with power on the fiber facet approximately 13.7 mW.

   Polystyrene beads were raster scanned by focusing a spot at the tip of the Sapphire fiber and then a Raman image was constructed by collecting the Raman signal as illustrated in Fig. 4. Raman image resolution depends on the spot size of the DPC spot. When the DPC spot is 30 μm away from the fiber, the spot size is 0.63 μm. During the calibration process, the step size for objective 2 was set to 0.5 μm. Thus, the DPC step is 0.5 μm for a fine resolution scanning or 1 μm for a rough resolution by sending different numbers of phase images to the SLM. Figure 4(a) -4(c) are measurements for multiple polystyrene beads, with total power on the beads 10-12 mW, and power on the DPC spot around 1.5-1.8 mW. Figure 4(a) and 4(d) are optical images taken by camera 2 with the illumination coming through the Sapphire fiber by the 532 nm laser. The image has speckle noise due to the interferences of the coherent laser light illumination. The scanning areas (yellow rectangles) of Fig. 4(a) and 4(d) are 30 μm × 30 μm, and 35 μm × 35 μm respectively.

   When the DPC spot focuses on the middle of the polystyrene bead in Fig. 4(a), the Raman spectrum was taken with an acquisition time of 30 s (Fig. 4(b)). The blue curve represents the background signal without any sample, while the red curve is the signal from the beads (with background subtracted). The bead's Raman signal at 1005.4 cm^{-1} is 3 times higher than the background signal from the Sapphire fiber. By comparison, with a silica fiber, the Raman signal is 10- 50 times [18] lower than the background at this frequency shift. Figure 4(c)

shows the Raman images at a shift of 1005.4 cm^{-1} with a 1 μm step. The morphology of the bead shapes can clearly be seen.

Figure 4(e) and 4(f) shows another Raman image of two beads with a scanning step of 0.5 μm. Figure 4(f) was taken 14 hours later than Fig. 4(e), which shows the stability of the system.
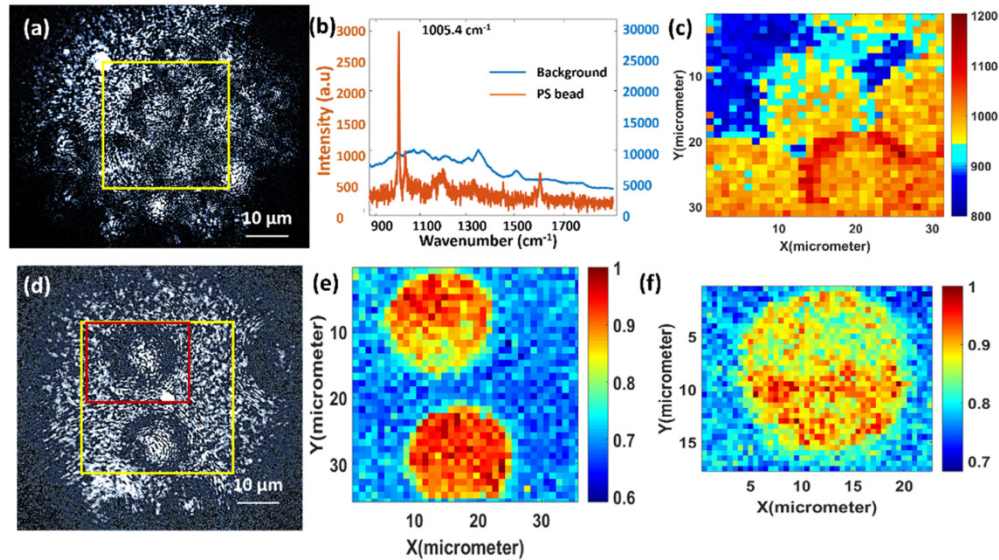

Fig. 4. Raman imaging of Polystyrene beads. (a) Optical image of multiple polystyrene beads (the speckled image comes from the coherent 532 nm illumination through the sapphire). (b) Raman spectrum of the beads in (a), when the DPC spots focus on one of the beads. (c) Raman image taken at 1005.4 cm^{-1} in the scanning area of 30 μm × 30 μm shown in (a), step size 1 μm. (d) Optical image of two polystyrene beads. (e) Raman image taken at 1005.4 obtained with scanning step 0.5 μm (f) Raman image of the single bead in (e) taken 14 hours later.

Figure 5(a) is a wide field image (obtained with white incoherent light) of a single polystyrene bead (round shape) and some CaSO$_4$ agglomerations (rectangle shape). The Raman shift of CaSO$_4$, which is 1011.1 cm^{-1}, is very close to that of the polystyrene bead with a Raman shift of 1005.4 cm^{-1}. Figure 5(b) is the Raman spectrum with the DPC spot in the middle of the bead. Although the DPC spot is located on the bead, there is a significant background light at 532 nm that is not in the Airy disk but rather distributed randomly. This background light generates also a Raman signal that is collected by the fiber. As can be seen, due to the background light, the Raman signal from CaSO$_4$ can also be detected. When DPC spot position changes, the ratio of the Raman peaks from the two materials is also changed. The scanning area is the yellow rectangle (22.5 μm × 15 μm) and the scanning step is 0.5 μm. The scanned Raman images obtained at the two Raman peaks are shown in Fig. 5(c) and 5(d), which differentiate clearly the polystyrene bead from the CaSO$_4$ agglomerations.
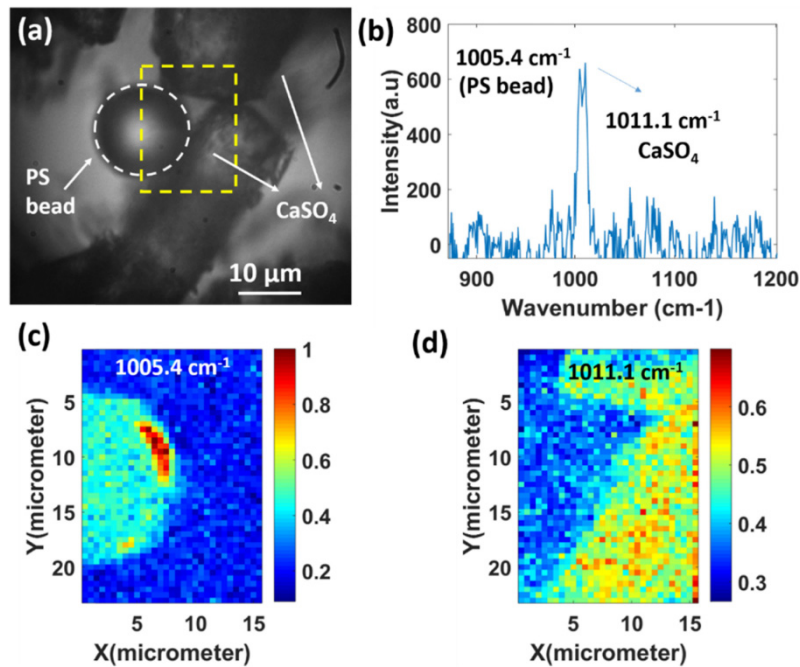
Fig. 5. Raman images of single polystyrene bead and $CaSO_4$ agglomerations. (a) Optical image of single polystyrene bead and $CaSO_4$ agglomerations with white light as illumination. (b) Raman spectrum of polystyrene bead (1005.4 cm^{-1}) and $CaSO_4$ agglomerations (1011.1 cm^{-1}). (c, d) Scanned Raman image taken at 1005.4 cm^{-1} and 1011.1 cm^{-1} respectively with scanning step 0.5 μm.

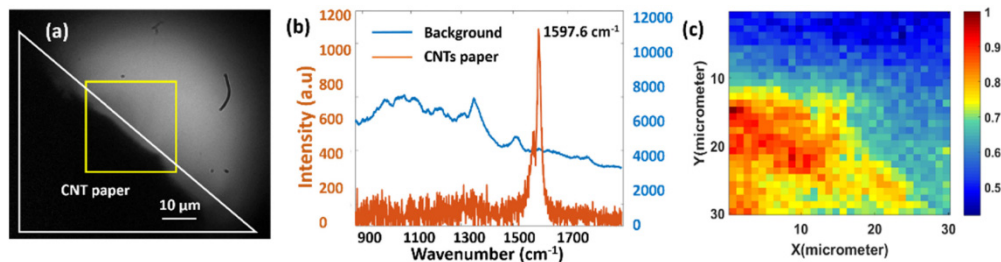Fig. 6. Raman imaging of Carbon Nanotube (CNT) paper. (a) Optical image of CNT paper. The yellow rectangle (30 μm × 30 μm) is the scanning area, with step 1 μm. (b) Raman spectrum when the DPC spot focus on CNT paper, with power around 12-14 mW, acquisition time 30 s. (c) Raman imaging of CNT paper reconstructed by the Raman peak 1597.6 cm^{-1}.

To show Raman imaging with our probe at longer frequency shifts, we used a sample of Carbon Nanotube (CNT) paper which exhibit a Raman shift at 1597.6 cm^{-1}. The optical image of CNT paper is illustrated in 6(a), with CNT paper located in the white delineated lower triangle. The edge of the CNT paper lies in the diagonal of the image. The scanning area (30 μm × 30 μm, step 1 μm) is shown in a yellow rectangle. The Raman spectrum with the DPC spot focused on the CNT paper is shown in comparison with the background in Fig. 6(b). The signal from CNT paper at 1597.6 cm^{-1} is twice that of the background. The Raman image in Fig. 6(c) matches well with the scanning area in Fig. 6(a). A Raman image of a single polystyrene bead together with CNT paper is shown in supplementary information S1.

4. Summary and conclusions

A sapphire fiber Raman imaging probe of diameter 60 micrometer, which can be used for endoscopic applications (in this case, a cladding will be required) and potentially for high temperature detections, is presented in this paper. This probe performs imaging without any mechanical motion and without any focusing optics at the tip, which makes it particularly interesting in harsh environments such as high temperature and/or in contact with corrosive liquids [29] and gases.

We have shown experimentally Raman imaging of samples including polystyrene beads, $CaSO_4$ agglomerations, and CNTs paper with a resolution of 0.6 um and field of view of 30 x 30 um in a Raman shift range between 1000 cm^{-1} and 1600 cm^{-1}. Compared with silica fibers, which restricts Raman imaging to frequency shifts beyond 1700 cm^{-1}, the sapphire fiber probe enables detection below this value. Potentially, detection in the low frequency shift region (0-300 cm^{-1}) should also be feasible with this probe due to the low background of sapphire.

We have shown excellent spatial chemical differentiation by imaging a mixture of polystyrene beads and $CaSO_4$ agglomerations at two distinct Raman shifts f with 1005.4 cm^{-1} and 1011.1 cm^{-1} respectively.

In this work, digital phase conjugation was used to scan a focal spot at the tip of a sapphire fiber. Other methods to scan a focused spot at the tip of the fiber could have been used, such as transmission matrix method. Because of the high number of modes (125'000), we have chosen to use the DPC technique. Such a high number of modes would create a matrix whose size could not be invertible with the desktop computer we used. The calibration of 40 μm $\times$ 40 μm area with resolution 0.5 μm takes approximately 2 hours. The time will increase with increased scanning area and resolution. A limitation of the proposed DPC focusing system is that the system needs to be calibrated point by point and thus calibration takes time. The DPC system needs to be carefully aligned with the same amount of angular tolerance as needed for coupling light into a single mode fiber. Thus, mechanical robustness is needed to keep the system aligned.

In summary, we demonstrated a sapphire fiber Raman probe for mapping materials in a broad fingerprint region. This multimode Sapphire fiber probe overcomes the limitations of silica fiber probes because of sapphire unique properties, including low fluorescence and Raman background and good stability in high temperature.

Acknowledgments

We would like to further thank Dr. Ye Pu, for useful discussions and review of the manuscript.

References

1. J. M. Surmacki, B. J. Woodhams, A. Haslehurst, B. A. J. Ponder, and S. E. Bohndiek, "Raman micro-spectroscopy for accurate identification of primary human bronchial epithelial cells," Sci. Rep. **8**(1), 12604 (2018).
2. R. S. Das, Y. K. Agrawal, "Raman spectroscopy: recent advancements, techniques and applications," Vib. Spectrosc. **57**(2), 163–176 (2011).
3. L. Shi, C. Zheng, Y. Shen, Z. Chen, E. S. Silveira, L. Zhang, M. Wei, C. Liu, C. de Sena-Tomas, K. Targoff, and W. Min, "Optical imaging of metabolic dynamics in animals," Nat. Commun. **9**(1), 2995 (2018).
4. S. Deng, L. Liu, Z. Liu, Z. Shen, G. Li, and Y. He, "Line-scanning Raman imaging spectroscopy for detection of fingerprints," Appl. Opt. **51**(17), 3701–3706 (2012).
5. L. V. Doronina-Amitonova, I. V. Fedotov, A. B. Fedotov, and A. M. Zheltikov, "High-resolution wide-field Raman imaging through a fiber bundle," Appl. Phys. Lett. **102**(16), 161113 (2013).

6. L. V. Doronina-Amitonova, I. V. Fedotov, A. B. Fedotov, K. V. Anokhin, M. L. Hu, C. Y. Wang, and A. M. Zheltikov, "Raman detection of cell proliferation probes with antiresonance-guiding hollow fibers," Opt. Lett. **37**(22), 4642–4644 (2012).

7. M. Jermyn, J. Desroches, K. Aubertin, K. St-Arnaud, W.-J. Madore, E. De Montigny, M.-C. Guiot, D. Trudel, B. C. Wilson, K. Petrecca, and F. Leblond, "A review of Raman spectroscopy advances with an emphasis on clinical translation challenges in oncology," Phys. Med. Biol. **61**(23), R370–R400 (2016).

8. I. Notingher and L. L. Hench, "Raman microspectroscopy: a noninvasive tool for studies of individual living cells in vitro," Expert Rev. Med. Devices **3**(2), 215–234 (2006).

9. C. Raml, X. He, M. Han, D. R. Alexander, and Y. Lu, "Raman spectroscopy based on a single-crystal sapphire fiber," Opt. Lett. **36**(7), 1287–1289 (2011).

10. B. Liu, Z. Yu, Z. Tian, D. Homa, C. Hill, A. Wang, and G. Pickrell, "Temperature dependence of sapphire fiber Raman scattering," Opt. Lett. **40**(9), 2041–2044 (2015).

11. H. Ahn, H. Song, D.-M. Shin, K. Kim, and J. Choi, "Emerging optical spectroscopy techniques for biomedical applications—A brief review of recent progress," Appl. Spectrosc. Rev. **53**(2-4), 264–278 (2018).

12. K. A. Esmonde-White, F. W. Esmonde-White, M. D. Morris, and B. J. Roessler, "Fiber-optic Raman spectroscopy of joint tissues," Analyst (Lond.) **136**(8), 1675–1685 (2011).

13. J. C. Day and N. Stone, "A subcutaneous Raman needle probe," Appl. Spectrosc. **67**(3), 349–354 (2013).

14. T. Yamanaka, H. Nakagawa, M. Ochida, S. Tsubouchi, Y. Domi, T. Doi, T. Abe, and Z. Ogumi, "Ultrafine fiber Raman probe with high spatial resolution and fluorescence noise reduction," J. Phys. Chem. C **120**(5), 2585–2591 (2016).

15. Y. Hattori, Y. Komachi, T. Asakura, T. Shimosegawa, G. Kanai, H. Tashiro, and H. Sato, "In vivo Raman study of the living rat esophagus and stomach using a micro-Raman probe under an endoscope," Appl. Spectrosc. **61**(6), 579–584 (2007).

16. I. E. Iping Petterson, J. C. Day, L. M. Fullwood, B. Gardner, and N. Stone, "Characterisation of a fibre optic Raman probe within a hypodermic needle," Anal. Bioanal. Chem. **407**(27), 8311–8320 (2015).

17. K. Ehrlich, A. Kufcsák, S. McAughtrie, H. Fleming, N. Krstajic, C. J. Campbell, R. K. Henderson, K. Dhaliwal, R. R. Thomson, and M. G. Tanner, "pH sensing through a single optical fibre using SERS and CMOS SPAD line arrays," Opt. Express **25**(25), 30976–30986 (2017).

18. I. Gusachenko, M. Chen, and K. Dholakia, "Raman imaging through a single multimode fibre," Opt. Express **25**(12), 13782–13798 (2017).

19. M. Kirsch, G. Schackert, R. Salzer, and C. Krafft, "Raman spectroscopic imaging for in vivo detection of cerebral brain metastases," Anal. Bioanal. Chem. **398**(4), 1707–1713 (2010).

20. P. Colomban, "Potential and drawbacks of Raman (micro) spectrometry for the understanding of iron and steel corrosion," in *New Trends and Developments in Automotive System Engineering* (InTech, 2011).

21. E. E. Morales-Delgado, S. Farahi, I. N. Papadopoulos, D. Psaltis, and C. Moser, "Delivery of focused short pulses through a multimode fiber," Opt. Express **23**(7), 9109–9120 (2015).

22. E. E. Morales-Delgado, D. Psaltis, and C. Moser, "Two-photon imaging through a multimode fiber," Opt. Express **23**(25), 32158–32170 (2015).

23. I. N. Papadopoulos, S. Farahi, C. Moser, and D. Psaltis, "Focusing and scanning light through a multimode optical fiber using digital phase conjugation," Opt. Express **20**(10), 10583–10590 (2012).

24. D. Loterie, S. Farahi, I. Papadopoulos, A. Goy, D. Psaltis, and C. Moser, "Digital confocal microscopy through a multimode fiber," Opt. Express **23**(18), 23845–23858 (2015).

25. D. Loterie, S. A. Goorden, D. Psaltis, and C. Moser, "Confocal microscopy through a multimode fiber using optical correlation," Opt. Lett. **40**(24), 5754–5757 (2015).

26. J. W. Czarske, D. Haufe, N. Koukourakis, and L. Büttner, "Transmission of independent signals through a multimode fiber using digital optical phase conjugation," Opt. Express **24**(13), 15128–15136 (2016).

27. N. Verrier and M. Atlan, "Off-axis digital hologram reconstruction: some practical considerations," Appl. Opt. **50**(34), H136–H146 (2011).

28. S. Deng, P. Penchev, J. Liu, Y. Wang, K. Jiang, S. Dimov, Z. Zhang, Y. Liu, J. Leng, and H. Butt, "Laser directed writing of flat lenses on buckypaper," Nanoscale **7**(29), 12405–12410 (2015).

29. I. Gusachenko, J. Nylk, J. A. Tello, and K. Dholakia, "Multimode fibre based imaging for optically cleared samples," Biomed. Opt. Express **8**(11), 5179–5190 (2017).